Anisotropic Debye model for the thermal boundary conductance

Z. Chen,[1] Z. Wei,[2] Y. Chen,[2] and C. Dames[1,*]

[1]*Department of Mechanical Engineering, University of California, Berkeley, California 94720, USA*

[2]*Jiangsu Key Laboratory for Design & Manufacture of Micro/Nano Biomedical Instruments and Department of Mechanical Engineering, Southeast University, Nanjing 210096, China*

Most standard models for the thermal boundary conductance (TBC) assume isotropic properties and thus are inappropriate for layered and chainlike materials such as graphite, Bi_2Te_3, and high-density polyethylene (HDPE). To model such anisotropic materials, here a framework is introduced whereby the first Brillouin zone and the isoenergy surfaces of the Debye dispersion relation are both generalized from spherical to ellipsoidal. This model is checked by comparison with the experimental specific heat capacity of graphite and HDPE, as well as the phonon irradiation of graphite calculated from lattice dynamics. The anisotropic TBC model performs at least six times better than the standard isotropic diffuse mismatch model at explaining the measured TBC between graphite and various metals reported by Schmidt *et al.* [J. Appl. Phys. **107**, 104907 (2010)]. The model further reveals an unexpected guideline to engineer the TBC: due to phonon focusing effects, in many cases the TBC across an interface can be increased by reducing a phonon velocity component parallel to the plane of the interface.

I. INTRODUCTION

Understanding and engineering the thermal boundary conductance (TBC, also discussed as a thermal boundary resistance or thermal contact resistance) across atomically intimate interfaces is becoming increasingly important as the characteristic lengths of modern devices continue shrinking to micro- and nanoscales.[1] Nearly all models for the TBC, such as the widely used diffuse mismatch model (DMM) and acoustic mismatch model (AMM),[2] require that the materials have isotropic properties and are most commonly based on an isotropic Debye dispersion relation. However, many important materials are highly anisotropic, including layered materials such as graphite, boron nitride, and Bi_2Te_3, and chainlike materials such as high-density polyethylene (HDPE). In such highly anisotropic materials, the conventional isotropic Debye model is no longer a good approximation. For example, in graphite at intermediate temperatures the predictions of the isotropic Debye model deviate from the experimental data for the specific heat capacity by more than a factor of 2,[3,4] and, as will be shown below, compared to the measured TBC between graphite and metals,[5] DMM calculations using an isotropic Debye model are typically in error by more than a factor of 10.

For the special case of interfaces involving graphite, recently two anisotropic TBC models were reported. Prasher[6] used the DMM to model the TBC between graphite and platinum below 100 K using the anisotropic graphite dispersion from Komatsu.[7] Also using the DMM, Duda *et al.*[8] modeled the TBC between graphite and aluminum by approximating graphite's density of states (DOS) as two dimensional (2D). In both cases the modeled TBC was found to be lower for interfaces oriented parallel to graphite's *ab* planes (also called basal planes), which was attributed to the fact that the sound velocity is much lower in the *c*-axis direction than along the *ab* planes. Because these models[6,8] were developed specifically for graphite, they are difficult to generalize to other anisotropic materials.

Here we develop a general framework for the TBC using an anisotropic Debye phonon dispersion, whereby the first Brillouin zone and the isoenergy surfaces are both generalized from spherical to ellipsoidal. We restrict the analysis to materials where only one of the three principle directions is anisotropic; that is, materials with tetragonal, trigonal, or hexagonal symmetries. This restriction is appropriate for a large number of layered and chainlike materials, including graphite, boron nitride, Bi_2Te_3, HDPE, and tellurium. This paper is organized as follows. In Sec. II we present the two basic assumptions of the framework and derive an expression for the TBC, including simple analytical expressions for several limiting cases. The specific heat capacity is also discussed. Then in Sec. III we compare the model to experimental results from the literature for the specific heat of a typical layered (graphite) and chainlike (HDPE) material, and for the TBC between graphite and various metals.

II. DESCRIPTION OF THE MODEL

A. Basic assumptions and justifications

The first key assumption of this model is that a material's anisotropic phonon dispersion can be well approximated by the anisotropic Debye dispersion, $\omega^2 = v_a^2 k_a^2 + v_b^2 k_b^2 + v_c^2 k_c^2$, where v_a, v_b, and v_c are the sound velocities along the *a*-, *b*-, and *c*-axis directions, respectively, and (k_a, k_b, k_c) is the wave vector. This dispersion has ellipsoidal isoenergy surfaces in k space [Fig. 1(a)]. Because in this work we focus on materials with $v_a = v_b = v_{ab}$, this simplifies to

$$\omega^2 = v_{ab}^2 k_{ab}^2 + v_c^2 k_c^2, \tag{1}$$

where $k_{ab}^2 = k_a^2 + k_b^2$.

The other key assumption is that an anisotropic material's first Brillouin zone (FBZ) can be adequately approximated by an ellipsoid [Fig. 1(b)], an obvious generalization of the spherical FBZ used in the classic isotropic Debye model. Here the FBZ ellipsoid is defined as the surface satisfying
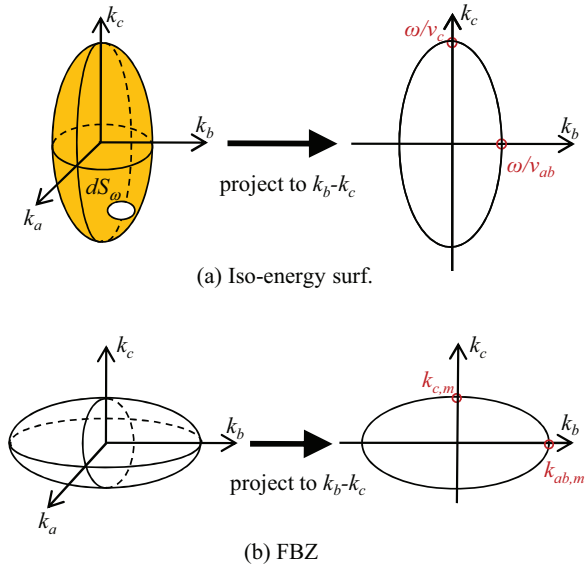
(a) Iso-energy surf.

(b) FBZ

FIG. 1. (Color online) (a) Isoenergy surface (here for $v_{ab} > v_c$; the opposite case is straightforward). The ellipsoidal surface has an equatorial radius ω/v_{ab} and polar radius ω/v_c. Its k_b-k_c projection is an ellipse. (b) FBZ (here for $k_{ab,m} > k_{c,m}$; the opposite case is straightforward) with equatorial radius $k_{ab,m}$ and polar radius $k_{c,m}$. Its k_b-k_c projection is also an ellipse.

$\frac{k_a^2}{k_{a,m}^2} + \frac{k_b^2}{k_{b,m}^2} + \frac{k_c^2}{k_{c,m}^2} = 1$, where $k_{a,m}$, $k_{b,m}$, and $k_{c,m}$ are wave-vector cutoffs. Because we focus on materials with restricted symmetries such that $k_{a,m} = k_{b,m} = k_{ab,m}$, this can be written

$$\frac{k_{ab}^2}{k_{ab,m}^2} + \frac{k_c^2}{k_{c,m}^2} = 1. \qquad (2)$$

To ensure the correct total number of acoustic modes, these wave-vector cutoffs are constrained by the number density of primitive unit cells η_{puc} through

$$\eta_{\text{puc}} = \frac{1}{6\pi^2} k_{ab,m}^2 k_{c,m}. \qquad (3)$$

The number of optical modes is given by $\eta_{\text{opt}} = 3(m - 1)\eta_{\text{puc}}$, where m is the number of atoms in the crystal basis. For simplicity we approximate them as Einstein modes, making their contributions to heat transfer vanish.

We now comment briefly on the validity of this anisotropic Debye approximation. The form of Eq. (1) is motivated by an exact result from continuum elasticity,[9–11] in which the dispersion relation for the pure transverse acoustic (pure-TA) branch of materials with hexagonal symmetry can be written as

$$\rho\omega^2 = C_{66}k_{ab}^2 + C_{44}k_c^2, \qquad (4)$$

where ρ is the mass density and C_{ij} is the stiffness constant. Although the dispersion relations for both the quasi-longitudinal acoustic (quasi-LA) and the quasi-transverse acoustic (quasi-TA) branches have more complicated angular dependencies,[11] under certain conditions they also are well approximated by the form of Eq. (4) using different C_{ij} (details in Sec. III A3). Graphite is a typical example satisfying these conditions. However, this anisotropic Debye approximation cannot capture the variation of the phase velocity with the

magnitude of the wave vector in real materials, which arises purely from atomistic effects.[12] For example, the present model cannot capture the curvature of the well-known flexural [ZA, also called TA$_\perp$ (Ref. 13) or oTA Ref. 14] branch in graphite, which has been given by Lifshitz as[12,15]

$$\rho\omega^2 = C_{44}k_{ab}^2 + C_{33}k_c^2 + \frac{B}{d}k_{ab}^4, \qquad (5)$$

where B is related to the bond-bending stiffness of an isolated graphene layer and d is the interlayer distance. The last term in Eq. (5) is a subcontinuum effect, which can be formally neglected if $k_{ab}^2 \ll C_{44}d/B$. Similar considerations apply to chainlike materials and the bond-bending stiffness of individual atomic chains.[12]

Comparing the anisotropic Debye model of Eq. (1) to the real dispersion of a typical layered material, graphite,[16] we estimate that for all three acoustic branches (LA, TA, ZA) the present model is in error by typically tens of percent for variations in ω with the magnitude of **k** in any fixed direction. This shortcoming is offset, however, by the merit of the model in capturing the large variations of ω with the direction of **k**, which is the emphasis of the present work. These directional variations can be substantial: for example, $\mathbf{v}_g$ in graphite changes by a factor of approximately 5–10, as estimated by comparing the sound velocity in the ab plane to that along the c axis. Section III will show that this anisotropic Debye approximation compares favorably with experimental values of the specific heat and a more detailed lattice dynamics calculation of phonon irradiation, typically to within ±10% over the temperature range 200–2000 K.

B. Characteristic frequencies and temperatures

Based on the ellipsoidal dispersion relation and FBZ, we define the characteristic Debye frequencies of the ab plane and c-axis directions,

$$\omega_{D,ab} = v_{ab}k_{ab,m}, \quad \omega_{D,c} = v_c k_{c,m}, \qquad (6)$$

with corresponding Debye temperatures

$$\theta_{D,ab} = \hbar\omega_{D,ab}/k_B, \quad \theta_{D,c} = \hbar\omega_{D,c}/k_B, \qquad (7)$$

where $\hbar$ is the reduced Planck's constant and k_B is the Boltzmann constant. It will also prove convenient to define the anisotropy ratio

$$r = \frac{\omega_{D,ab}}{\omega_{D,c}} = \frac{\theta_{D,ab}}{\theta_{D,c}}. \qquad (8)$$

We refer to materials with $r > 1$ as "layered" and $r < 1$ as "chainlike." Thus graphite ($r \gg 1$) is strongly layered, while HDPE is strongly chainlike ($r \ll 1$).

The definitions of Eqs. (6)–(8) facilitate the upcoming analysis by distinguishing between two different frequency regimes, as shown in Fig. 2. First, for those modes with $\omega < \min(\omega_{D,c}, \omega_{D,ab})$, the isoenergy surface has not reached the FBZ boundary, so all of those states are allowed as indicated by orange shading in Fig. 2(a). Second, for those modes with $\min(\omega_{D,c}, \omega_{D,ab}) < \omega < \max(\omega_{D,c}, \omega_{D,ab})$, part of the isoenergy surface lies outside of the FBZ, so only the part inside the FBZ is allowed [orange shading in Fig. 2(b)].

(a) $\omega < \omega_{D,c}$

(b) $\omega_{D,c} < \omega < \omega_{D,ab}$
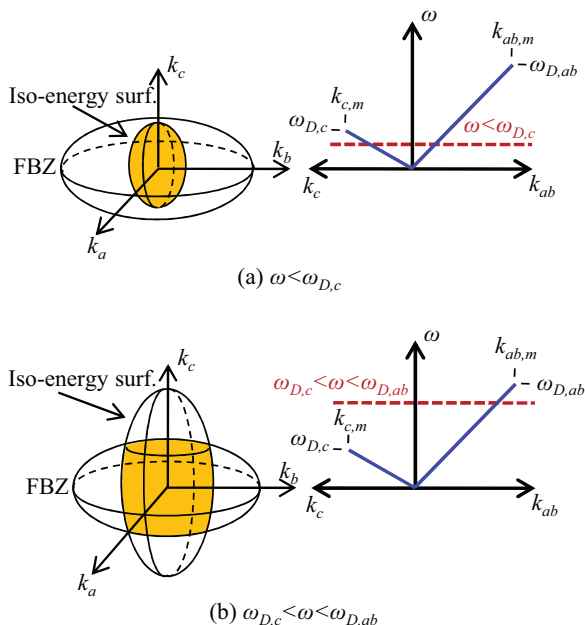
FIG. 2. (Color online) Two frequency regimes (here for $v_{ab} > v_c$, and $k_{ab,m} > k_{c,m}$; the other combinations are straightforward). (a) When $\omega < \min(\omega_{D,c}, \omega_{D,ab})$, all of the states on the isoenergy surface are allowed. (b) When $\min(\omega_{D,c}, \omega_{D,ab}) < \omega < \max(\omega_{D,c}, \omega_{D,ab})$, only the states inside the FBZ are allowed. In both cases the orange shading indicates the allowed states.

C. Specific heat

The phonon specific heat is given by

$$C = \sum_{\text{pol}} \int \hbar\omega \frac{\partial f_{BE}}{\partial T} D(\omega) d\omega, \qquad (9)$$

where the sum runs over all polarizations, f_{BE} is the Bose-Einstein distribution function, and $D(\omega)$ is the DOS which for an arbitrary dispersion relation is given by[17]

$$D(\omega) = \frac{1}{8\pi^3} \iint \frac{dS_\omega}{\|\mathbf{v}_g\|}, \qquad (10)$$

where dS_ω is an elemental area on an isoenergy surface in k space [Fig. 1(a)]. For the anisotropic Debye model defined by Eqs. (1) and (2), the analytical expression of DOS is conveniently evaluated in two regimes depending on the anisotropy ratio r (details in Appendix A).

In Fig. 3, we plot the dimensionless density of states $\hat{D} = D(\omega_{D,ab}^2 \omega_{D,c})^{\frac{1}{3}}/(3\eta_{\text{puc}})$ as a function of the dimensionless frequency $\hat{\omega} = \omega/(\omega_{D,ab}^2 \omega_{D,c})^{\frac{1}{3}}$ for a single polarization. The key feature is the range of power laws describing $\hat{D}$ versus $\hat{\omega}$. The isotropic "control" case ($r = 1$) follows the well-known quadratic power law over the entire frequency range. Layered materials ($r \gg 1$) show a transition from a quadratic to a linear power law with increasing ω, which can be interpreted by the scenario depicted in Fig. 2(b). This transition indicates a dimensionality crossover from 3D to 2D as the c-axis modes become fully saturated at large ω. Chainlike materials ($r \ll 1$), on the other hand, show a transition from a quadratic to a
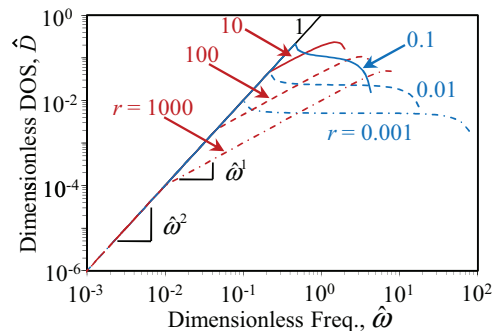

FIG. 3. (Color online) Dimensionless DOS, $\hat{D} = D(\omega_{D,ab}^2 \omega_{D,c})^{\frac{1}{3}}/(3\eta_{\text{puc}})$, as a function of dimensionless frequency $\hat{\omega} = \omega/(\omega_{D,ab}^2 \omega_{D,c})^{\frac{1}{3}}$. While layered materials ($r \gg 1$) show a transition from a quadratic to a linear power law with increasing ω, chainlike materials ($r \ll 1$) show a transition from a quadratic power law to a constant value. These transitions indicate different dimensionality crossovers.

power law to a constant value with increasing ω, indicating a dimensionality crossover from 3D to 1D.

Substituting Eqs. (A4) and (A5) into Eq. (9), we obtain two integral expressions for the specific heat in terms of $x = \hbar\omega/k_B T$. For $r > 1$,

$$C = \sum_{\text{pol}} \frac{k_B^4}{2\pi^2 v_{ab}^2 v_c \hbar^3} \Bigg[\int_0^{x_{D,c}} \frac{T^3 x^4 e^x}{(e^x - 1)^2} dx$$
$$+ \int_{x_{D,c}}^{x_{D,ab}} \frac{T^2 x^3 e^x}{(e^x - 1)^2} \sqrt{\theta_{D,c}^2 \frac{\theta_{D,ab}^2 - (Tx)^2}{\theta_{D,ab}^2 - \theta_{D,c}^2}} dx \Bigg], \quad (11a)$$

while for $r < 1$,

$$C = \sum_{\text{pol}} \frac{k_B^4}{2\pi^2 v_{ab}^2 v_c \hbar^3} \Bigg\{ \int_0^{x_{D,ab}} \frac{T^3 x^4 e^x}{(e^x - 1)^2} dx$$
$$+ \int_{x_{D,ab}}^{x_{D,c}} \Bigg[\frac{T^3 x^4 e^x}{(e^x - 1)^2} - \frac{T^2 x^3 e^x}{(e^x - 1)^2}$$
$$\times \sqrt{\theta_{D,c}^2 \frac{(Tx)^2 - \theta_{D,ab}^2}{\theta_{D,c}^2 - \theta_{D,ab}^2}} \Bigg] dx \Bigg\}. \quad (11b)$$

In both Eqs. (11a) and (11b), the first integral is the exact result for a traditional isotropic Debye solid, while the second integral captures the effects of anisotropy. Figure 4 shows the dimensionless specific heat $\hat{C} = C/(3\eta_{\text{puc}} k_B)$ versus the dimensionless temperature $\hat{T} = T/(\theta_{D,ab}^2 \theta_{D,c})^{\frac{1}{3}}$, calculated by numerical integration of Eqs. (11a) and (11b). Layered materials ($r \gg 1$) exhibit a transition from $T^3 \to T^2 \to T^0$ behavior with increasing T, while chainlike materials with $r \ll 1$ exhibit a transition from $T^3 \to T^1 \to T^0$. We will come back to these transitions in Sec. III B when comparing this model to the experimental specific heat of graphite and prior models.

To gain further physical insight, in Table I we simplify Eqs. (11a) and (11b) in several limiting cases. First, in the low-temperature limit [$T \ll \min(\theta_{D,c}, \theta_{D,ab})$], only low-energy phonons are activated, in which case the FBZ boundaries are far away from the isoenergy surfaces [Fig. 1(a)]. Therefore the analytical expression recovers the classic Debye T^3 law and
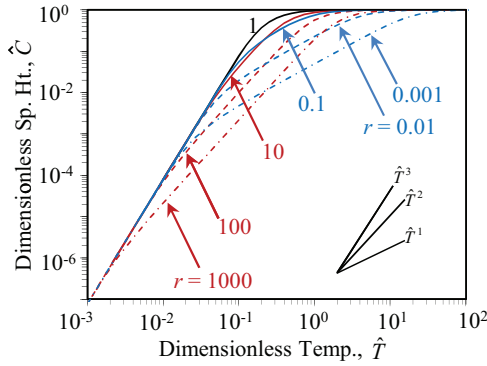
FIG. 4. (Color online) Dimensionless specific heat, $\hat{C} = C/(3\eta_{\text{puc}}k_B)$, as a function of dimensionless temperature, $\hat{T} = T/(\theta_{D,ab}^2\theta_{D,c})^{\frac{1}{3}}$, obtained by numerical integration of Eqs. (11a) and (11b). All materials recover the Debye T^3 law at low T, and Dulong and Petit limit at high T. But at intermediate temperatures the layered materials ($r \gg 1$) show a T^2 dependence, while the chainlike materials ($r \ll 1$) show a T^1 dependence.

depends on the two sound velocities, but not the two wave-vector cutoffs because the phonon wavelengths are insensitive to the granularity of the lattice in this limit. On the other hand, in the high-temperature limit [$T \gg \max(\theta_{D,c}, \theta_{D,ab})$], all of the phonons are fully activated and obey equipartition of energy. Thus the analytical expression recovers the Dulong and Petit result and depends on the two wave-vector cutoffs (related to the total number of phonon modes) but not the sound velocities.

At intermediate temperatures [$\min(\theta_{D,c}, \theta_{D,ab}) \ll T \ll \max(\theta_{D,c}, \theta_{D,ab})$], Table I shows that strongly anisotropic materials exhibit a mixture of the high-T and low-T behaviors just described. At intermediate T, the populated isoenergy surfaces reach the FBZ boundary along the crystal direction of low sound velocity, while remaining far from the FBZ boundary along the direction of fast sound velocity [Fig. 1(b)]. Therefore the slow-velocity direction is saturated in its high-T regime while the fast-velocity direction is still in its low-T regime. Thus the limiting analytical expression for a layered material at intermediate temperature follows a T^2 power law, and depends on v_{ab} and $k_{c,m}$ but not v_c or $k_{ab,m}$. Conversely, a chainlike material follows a T^1 law, and depends on v_c and $k_{ab,m}$ but not v_{ab} or $k_{c,m}$. These intermediate T behaviors

are further justified in Appendix B through an alternative derivation using simplified two- and one-dimensional (2D and 1D) phonon gas models.

D. Phonon irradiation

We calculate the irradiation and TBC using the close analogy between phonon transport and photon radiation. We restrict the analysis to interfaces oriented normal to the material's c axis, the configuration of highest symmetry, because this simplifies the analysis and it is also a common configuration in applications and experiments.[5] For materials with isotropic properties, the "incident radiation" [Eq. (6) of Ref. 18] is a convenient quantity for evaluating the TBC. However, to accommodate materials with anisotropic properties, the phonon "irradiation" is a better choice. A general expression for the irradiation along the c axis is

$$H_c = \sum_{\text{pol}} \iiint_{\mathbf{k}\cdot\hat{\mathbf{c}}<0} I\hat{\mathbf{s}} \cdot \hat{\mathbf{c}}\, d^3\mathbf{k}, \qquad (12)$$

where $\hat{\mathbf{c}} = (0,0,1)$ is the unit vector along the c axis, $\hat{\mathbf{s}}$ is a unit vector parallel to the group velocity, $\mathbf{k} \cdot \hat{\mathbf{c}} < 0$ denotes integration over the incident half space, and the intensity $I = \frac{1}{8\pi^3}\hbar\omega\|\mathbf{v}_g\|f_{BE}$ at wave vector $\mathbf{k}$ travels in the $\hat{\mathbf{s}}$ direction.

It is helpful to convert Eq. (12) to an integral over frequency,

$$H_c = \sum_{\text{pol}} \int_\omega \hbar\omega h_c f_{BE}\, d\omega, \qquad (13)$$

where we introduce a new quantity h_c, which can be understood as the density of states [Eq. (10)] weighted by the c-axis projected velocity:

$$h_c(\omega) = \frac{1}{8\pi^3} \iint_{\hat{\mathbf{s}}\cdot\hat{\mathbf{c}}<0} \frac{(\mathbf{v}_g \cdot \hat{\mathbf{c}})}{\|\mathbf{v}_g\|}\, dS_\omega. \qquad (14)$$

Thus h_c represents the product of the phonon velocity component along the direction of heat transfer (here, $\hat{\mathbf{c}}$) and the number of phonon modes per unit frequency between ω and $\omega + d\omega$, integrated over the incident half-FBZ. We refer to h_c as the vDOS (v indicating velocity-weighted), and its role in the irradiation [Eq. (13)] is analogous to the role of the DOS in the specific heat [Eq. (9)]. Analytical expressions for the vDOS are given in Appendix A.

TABLE I. Analytical expressions for the specific heat in several limiting cases. The model recovers the Debye T^3 law in the low-temperature limit, and the Dulong and Petit law in the high-temperature limit. For strongly anisotropic materials at intermediate temperatures, the model predicts a T^2 dependence and T^1 dependence for layered ($r \gg 1$) and chainlike ($r \ll 1$) materials, respectively. $\zeta_3 = 1.202...$ is Apery's constant.

Low T		
$T \ll \min(\theta_{D,c}, \theta_{D,ab})$		$C_{\text{Low}T} = \frac{2\pi^2 k_B^4}{15\hbar^3}\sum_{\text{pol}}\frac{T^3}{v_{ab}^2 v_c}$
Intermediate T	Layered ($r \gg 1$)	Chainlike ($r \ll 1$)
$\min(\theta_{D,c}, \theta_{D,ab}) \ll T \ll \max(\theta_{D,c}, \theta_{D,ab})$	$C_{\text{Layer}-\text{Mid}T} = \frac{3\zeta_3 k_B^3 k_{c,m}}{\pi^2\hbar^2}\sum_{\text{pol}}\frac{T^2}{v_{ab}^2}$	$C_{\text{Chain}-\text{Mid}T} = \frac{k_{ab,m}^2 k_B^2}{12\hbar}\sum_{\text{pol}}\frac{T}{v_c}$
High T		
$T \gg \max(\theta_{D,c}, \theta_{D,ab})$		$C_{\text{High}T} = 3\eta_{\text{puc}}k_B$

Figure 5 shows the dimensionless vDOS, $\hat{h}_c = h_c \omega_{D,c}/(3\eta_{\text{puc}} v_c/4)$, versus the dimensionless frequency, $\hat{\omega} = \omega/\omega_{D,c}$, for a single polarization. Both layered and chainlike materials show a transition from a $\hat{\omega}^2$ dependence at low frequency to a constant value at high frequency. The low-frequency behavior is straightforward from Eqs. (A6) and (A7) of Appendix A, and the high-frequency behavior can be understood from the definition of h_c [Eq. (14)]: an averaged product of DOS [Eq. (10)] and the c-axis component of the group velocity. For layered materials, the high-frequency DOS is 2D and is thus proportional to ω (Fig. 3), and as shown in Appendix B, the frequency-dependent c-axis component of the group velocity scales as $v_{g,c,2D} \propto \omega^{-1}$. However, for chainlike materials, the high-frequency DOS is 1D and thus constant while $v_{g,c,1D} \propto \omega^0$ (Appendix B).

Substituting Eqs. (A6) and (A7) into Eq. (13), we obtain expressions for the irradiation. For $r > 1$,

$$H_c = \sum_{\text{pol}} \frac{k_B^4}{8\pi^2 v_{ab}^2 \hbar^3} \left\{ \int_0^{x_{D,c}} \frac{T^4 x^3}{e^x - 1} dx + \int_{x_{D,c}}^{x_{D,ab}} \left[\frac{\theta_{D,ab}^2 \theta_{D,c}^2}{\theta_{D,ab}^2 - \theta_{D,c}^2} \frac{T^2 x}{e^x - 1} - \frac{\theta_{D,c}^2}{\theta_{D,ab}^2 - \theta_{D,c}^2} \frac{T^4 x^3}{e^x - 1} \right] dx \right\}, \tag{15a}$$

while for $r < 1$,

$$H_c = \sum_{\text{pol}} \frac{k_B^4}{8\pi^2 v_{ab}^2 \hbar^3} \left\{ \int_0^{x_{D,ab}} \frac{T^4 x^3}{e^x - 1} dx + \int_{x_{D,ab}}^{x_{D,c}} \left[\frac{\theta_{D,c}^2 \theta_{D,ab}^2}{\theta_{D,c}^2 - \theta_{D,ab}^2} \frac{T^2 x}{e^x - 1} - \frac{\theta_{D,ab}^2}{\theta_{D,c}^2 - \theta_{D,ab}^2} \frac{T^4 x^3}{e^x - 1} \right] dx \right\}. \tag{15b}$$

The first integral of Eqs. (15a) and (15b) is the exact result for a traditional isotropic Debye solid, while the second integral captures the effects of anisotropy. In Fig. 6 we plot the dimensionless irradiation $\hat{H}_c = H_c/(3\eta_{\text{puc}}k_B v_c \theta_{D,c}/4)$ versus the dimensionless temperature $\hat{T} = T/\theta_{D,c}$. Both layered ($r \gg 1$) and chainlike ($r \ll 1$) materials show a $T^4 \to T^2 \to T^1$ transition with increasing T.

For further physical insight, Table II presents simplifications of Eqs. (15a) and (15b) for several limiting cases. In the low-temperature limit, regardless of r, Eqs. (15a) and (15b) reduce to the well-known blackbody emissive power law with a phonon Stephen-Boltzmann constant $\sigma_{\text{phonon}} = \pi^2 k_B^4 (\sum_{\text{pol}} v_{ab}^{-2})/(120\hbar^3)$.[19] In the limit of strongly anisotropic materials at intermediate temperatures, Table II shows that both layered and chainlike materials follow a T^2 power law, which arises from the power law $\hat{h}_c \propto \hat{\omega}$ (Fig. 5). These intermediate-temperature behaviors are further justified in Appendix B using simplified 2D and 1D phonon gas models.

Table II reveals the unexpected result that the c-axis irradiation H_c is generally *increased* by *reducing* the ab-plane sound velocity v_{ab} (the only exception being chainlike materials at intermediate T, for which H_c has no velocity dependence at all). This v_{ab} dependence of H_c can be understood as a consequence of phonon focusing.[20–22] As can be seen from Fig. 1(a), reducing v_{ab} elongates the isoenergy surfaces ("slowness surfaces" in Ref. 20) along the ab plane, thus increasing the component of the group velocity along the c-axis direction and correspondingly increasing H_c. This suggests a surprising guideline for materials engineering to increase TBC: the heat transfer along the c-axis direction can be *increased* by *reducing* a phonon velocity, as long as it is a velocity component perpendicular to the c axis. The analogous effect on the thermal conductivity of highly anisotropic materials has also been reported.[23–25] For example, a hybrid model[22] (lattice dynamics + molecular dynamics) confirmed that the thermal conductivity in the c-axis direction of a graphitelike material is also increased by reducing the ab-plane phonon velocity, caused in part by the same phonon
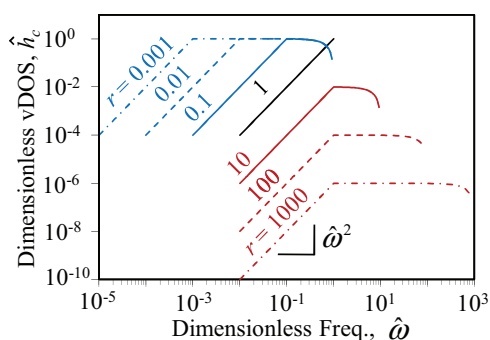

FIG. 5. (Color online) Dimensionless vDOS defined in Eq. (14), $\hat{h}_c = h_c \omega_{D,c}/(3\eta_{\text{puc}} v_c/4)$, as a function of dimensionless frequency, $\hat{\omega} = \omega/\omega_{D,c}$. Both layered ($r \gg 1$) and chainlike ($r \ll 1$) materials transition from a quadratic power law at low frequency to a constant value at high frequency.
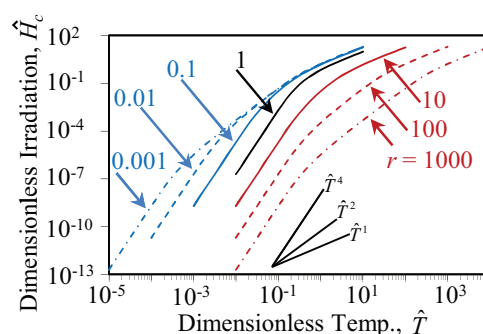

FIG. 6. (Color online) Dimensionless c-axis irradiation, $\hat{H}_c = H_c/(3\eta_{\text{puc}}k_B v_c \theta_{D,c}/4)$, as a function of dimensionless temperature, $\hat{T} = T/\theta_{D,c}$, obtained by numerical integration of Eqs. (15a) and (15b). Both layered ($r \gg 1$) and chainlike ($r \ll 1$) materials show $T^4 \to T^2 \to T^1$ power-law transitions.

TABLE II. Analytical expressions for the c-axis irradiation H_c in several limiting cases. In the low-temperature limit the model reduces to the blackbody emissive power law. For intermediate temperatures and strongly anisotropic materials, the model predicts a T^2 dependence for both layered and chainlike materials. These expressions also highlight the phonon focusing effect of the ab-plane velocity v_{ab}: except for chainlike materials at intermediate T, in all other cases H_c is actually increased by reducing v_{ab}.

Low T		
$T \ll \min(\theta_{D,c}, \theta_{D,ab})$		$H_{c-\text{Low}T} = \sigma_{\text{phonon}} T^4 = \left[\frac{\pi^2 k_B^4}{120\hbar^3} \sum_{\text{pol}} \frac{1}{v_{ab}^2} \right] T^4$
Intermediate T	**Layered ($r \gg 1$)**	**Chainlike ($r \ll 1$)**
$\min(\theta_{D,c}, \theta_{D,ab}) \ll T \ll \max(\theta_{D,c}, \theta_{D,ab})$	$H_{c-\text{Layer}-\text{Mid}T} = \frac{k_{c,m}^2 k_B^2 T^2}{48\hbar} \sum_{\text{pol}} \frac{v_c^2}{v_{ab}^2}$	$H_{c-\text{Chain}-\text{Mid}T} = \frac{k_{ab,m}^2 k_B^2 T^2}{16\hbar}$
High T		
$T \gg \max(\theta_{D,c}, \theta_{D,ab})$		$H_{c-\text{High}T} = \frac{1}{2} \eta_{\text{puc}} k_B T \sum_{\text{pol}} \frac{v_c k_{c,m}}{v_{ab} k_{ab,m} + v_c k_{c,m}} v_c$

focusing effects of interest here. In Sec. III, we will examine this anticipated H_c dependence of the TBC further for two particular models of transmission coefficient.

E. Thermal boundary conductance

From traditional radiative heat transfer,[26] the net heat flux across an interface between materials A and B can be expressed as

$$q = \tau[H_A(T_1)t_{AB}(T_1) - H_B(T_2)t_{BA}(T_2)], \quad (16)$$

where t_{AB} is an average (with respect to direction, position, energy, and polarization) transmission coefficient from A to B, T_1 and T_2 are the local equilibrium temperatures on either side of the interface, and the prefactor

$$\tau = \frac{1}{1 - \frac{1}{2}[t_{AB}(T_1) + t_{BA}(T_2)]} \quad (17)$$

arises because we work in terms of equilibrium rather than emitted temperatures (Appendix C).[18,27]

When the system is at equilibrium at temperature T, the second law of thermodynamics requires $q = 0$ and thus[2,18,28] from Eq. (16),

$$H_A(T)t_{AB}(T) = H_B(T)t_{BA}(T). \quad (18)$$

Substituting Eq. (18) into Eq. (16) and expanding q as a Taylor series in $\Delta T = T_1 - T_2$, we obtain an expression for the thermal boundary conductance defined as $G = \lim_{\Delta T \to 0}(q/\Delta T)$:

$$G = \tau \left[\frac{\partial H_i}{\partial T} t_{ij} + \frac{\partial t_{ij}}{\partial T} H_i \right], \quad (19)$$

where $i, j = A, B$ or equivalently B, A.

We note in passing that the TBC obtained from the limit $\Delta T \to 0$ must be always symmetric upon exchanging the labels A and B. Thus there cannot be any rectification in this low-bias regime, regardless of the model of the transmission coefficient. Although some analyses may neglect the second term of Eq. (19), such an approximation can have the side effect of incorrectly implying thermal rectification.[29]

III. COMPARISON WITH EXPERIMENTS

A. Specifying input parameters

1. Wave-vector cutoffs: $k_{ab,m}$ and $k_{c,m}$

Given η_{puc} for a real material, Eq. (3) sets the first constraint for the two wave-vector cutoffs, and as the second constraint we choose to fix the anisotropy ratio:

$$\frac{k_{ab,m}}{k_{c,m}} = \frac{k_{ab,m,\text{expt}}}{k_{c,m,\text{expt}}}, \quad (20)$$

where $k_{ab,m,\text{expt}}$ and $k_{c,m,\text{expt}}$ are wave-vector cutoffs consistent with the experimentally determined crystallographic structure. For example, one simple way to fix the $k_{m,\text{expt}}$ values is from the reported extents of the FBZ in the [100], [010], and/or [001] directions.

2. Sound velocities

We have used two different approaches to obtain the six sound velocities (three polarizations each of v_{ab} and v_c). The first and easiest approach is to use experimentally measured values along suitable high-symmetry directions in the ab plane and along the c axis. For materials for which the full phonon dispersion relation is available, a second approach is a "secant" method, in which case the sound velocity for a specified branch and direction is set to be equal to the slope of the secant that connects the Γ point and the end point of that branch at the FBZ boundary.

Although we could easily calculate the specific heat by summing over each branch (LA, TA$_1$, TA$_2$), for simplicity and physical insight it is also helpful to lump these six velocities into two effective ones, $v_{ab,\text{eff}}$ and $v_{c,\text{eff}}$, requiring two more equations. For the first constraint we insist on the correct low-T behavior of the specific heat from Table I, leading to

$$\frac{3}{v_{ab,\text{eff}}^2 v_{c,\text{eff}}} = \sum_{\text{pol}} \frac{1}{v_{ab}^2 v_c}. \quad (21)$$

Similarly, for the second constraint we require the correct intermediate-T behavior from Table I. For layered materials
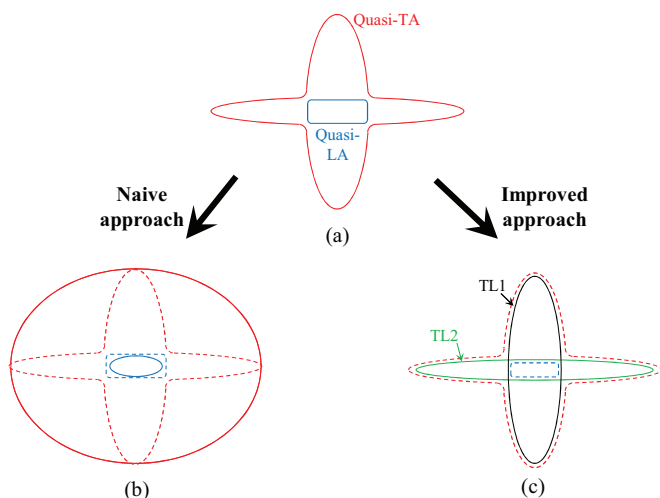
FIG. 7. (Color online) Debye ellipsoid approximations for the isoenergy surfaces of materials with hexagonal symmetry. The schematics represent projections in the A-Γ-M plane (an A-Γ-K plane looks very similar). (a) Schematic isoenergy surfaces for a graphitelike material with a lobed quasi-TA branch and an almost cylindrical quasi-LA branch. The third branch (pure TA) is not shown because it is already well approximated by an ellipsoid [Eq. (4)]. (b) A naive approach approximates the quasi-TA with a circumscribed ellipsoid and the quasi-LA with an inscribed ellipsoid. (c) An improved approach, used in this work, decomposes the quasi-TA and quasi-LA branches and then recomposes them as the two ellipsoids TL1 (black) and TL2 (green); see Eq. (25). The original and recomposed isoenergy surfaces in (c) have been offset slightly for clarity.

this gives

$$\frac{3}{v_{ab,\mathrm{eff}}^2} = \sum_{\mathrm{pol}} \frac{1}{v_{ab}^2}, \tag{22a}$$

while for chainlike materials we find

$$\frac{3}{v_{c,\mathrm{eff}}} = \sum_{\mathrm{pol}} \frac{1}{v_c}. \tag{22b}$$

Note that Eq. (21) is exact for all materials, but Eqs. (22a) and (22b) are exact only for highly anisotropic materials.

3. Decomposition of isoenergy surfaces for materials with hexagonal symmetry

As discussed in Sec. II A, the exact dispersion relations of the quasi-TA and quasi-LA branches are more complicated than Eq. (1), whether evaluated by lattice dynamics[22] or continuum elasticity [Eqs. (3.11) and (3.12) in the appendix of Ref. 11]. For a strongly layered material like graphite, the typical shapes of the exact isoenergy surfaces are depicted in Fig. 7(a). In the A-Γ-M plane, the quasi-LA surface is nearly rectangular while the quasi-TA surface has four prominent lobes (an A-Γ-K slice looks very similar).

The task here is to determine the best approximation of these isoenergy surfaces with Debye ellipsoids such as Fig. 1(a), given the principal sound velocities. The obvious but naive approach is to approximate each branch with its own ellipsoid. As indicated in Fig. 7(b), this is equivalent to approximating

the lobed quasi-TA branch with a circumscribed ellipsoid. Similarly, the quasi-LA would be replaced with an equivalent inscribed ellipsoid. As suggested by the graphical comparison of Fig. 7(b), these approximations appear quite crude and will introduce large errors in the phonon transport calculations. For example, for graphite at room temperature, H_C calculated in this way is 8 times too small as compared to that calculated using an all-direction lattice dynamics method as described in Appendix D.

A much improved approach is motivated by the exact dispersion relations of the quasi-TA and quasi-LA branches. From Eqs. (3.11) and (3.12) of the appendix of Auld,[11] when $(\frac{C_{13}}{C_{44}} + 1)^2 \ll (\frac{C_{11}}{C_{44}} - 1)(\frac{C_{33}}{C_{44}} - 1)$ it can be shown that

$$\omega_{\mathrm{quasi-TA}}^2 = \begin{cases} \frac{C_{11}}{\rho}k_{ab}^2 + \frac{C_{44}}{\rho}k_c^2, & \left|\frac{k_{ab}}{k_c}\right| \leqslant \sqrt{\frac{C_{33}-C_{44}}{C_{11}-C_{44}}} \\ \frac{C_{44}}{\rho}k_{ab}^2 + \frac{C_{33}}{\rho}k_c^2, & \left|\frac{k_{ab}}{k_c}\right| \geqslant \sqrt{\frac{C_{33}-C_{44}}{C_{11}-C_{44}}} \end{cases} \tag{23}$$

and

$$\omega_{\mathrm{quasi-LA}}^2 = \begin{cases} \frac{C_{11}}{\rho}k_{ab}^2 + \frac{C_{44}}{\rho}k_c^2, & \left|\frac{k_{ab}}{k_c}\right| \geqslant \sqrt{\frac{C_{33}-C_{44}}{C_{11}-C_{44}}} \\ \frac{C_{44}}{\rho}k_{ab}^2 + \frac{C_{33}}{\rho}k_c^2, & \left|\frac{k_{ab}}{k_c}\right| \leqslant \sqrt{\frac{C_{33}-C_{44}}{C_{11}-C_{44}}} \end{cases}. \tag{24}$$

Graphite satisfies this very well, $[(\frac{C_{13}}{C_{44}} + 1)^2 / (\frac{C_{11}}{C_{44}} - 1)(\frac{C_{33}}{C_{44}} - 1) < 0.01]$. Noticing the complementary relation between Eqs. (23) and (24), we rewrite them as two new branches,

$$\omega_{TL1}^2 = \frac{C_{11}}{\rho}k_{ab}^2 + \frac{C_{44}}{\rho}k_c^2,$$
$$\omega_{TL2}^2 = \frac{C_{44}}{\rho}k_{ab}^2 + \frac{C_{33}}{\rho}k_c^2, \tag{25}$$

with the graphical interpretation given in Fig. 7(c): decompose the lobed quasi-TA branch and the curved quadrilateral quasi-LA branch, and recompose them as two ellipsoids. Now all three branches of materials with hexagonal symmetry have dispersions in the form Eq. (1), and thus ellipsoidal isoenergy surfaces. To help validate this ellipsoidal Debye approximation, in Appendix D we compare its H_c with that from a full lattice-dynamics calculation of a graphitelike material. As shown in Fig. 12, the two calculations agree very well, to within $\pm10\%$ over a wide temperature range from 200 to 10 000 K.

4. Contributions from optical phonons

For materials with a polyatomic basis we use an Einstein model to account for the contributions of optical phonons, with Einstein frequencies taken from the average of the experimentally reported optical phonon frequencies at the Γ point and the edge of FBZ. Note that this treatment may be oversimplified for materials with complicated optical branches and/or optical phonons with large group velocities.

B. Specific heat of graphite

The specific heat of graphite has been well understood for decades both theoretically and experimentally,[3,4,7,9,12,13,30] making this a useful check of the accuracy of the anisotropic Debye approximation used in the present work. Graphite is

TABLE III. Input parameters for graphite, which are extracted from the phonon dispersion in Ref. 16 using the isoenergy-decomposition process described in Sec. III A3.

Parameter	Unit	ab plane	c axis
v_{TA}	m/s	10 200	1000
v_{TL1}	m/s	16 200	1000
v_{TL2}	m/s	6400	2500
k_{max}	10^{10} m^{-1}	1.73	1.1
$f_{E,\mathrm{LO/TO}}$	THz		42
$f_{E,\mathrm{ZO}}$	THz		23

highly anisotropic (r ranging from 10 to 16, depending on the polarization) and also has relevance for its close cousins graphene and carbon nanotubes.

Following the recipes outlined above, the input parameters are extracted from the published phonon dispersion[16] and summarized in Table III. We assign the secant velocity to all branches. In addition, to facilitate the analysis we unfold the dispersion relation along the c-axis direction:[6] in real space we cut the four-atom-basis primitive unit cell in half along the c axis to form a unit cell with a two-atom basis, and correspondingly, in reciprocal space the wave-vector cutoff $k_{c,m}$ is doubled. Only the c-axis direction was unfolded because the real dispersion relation[13,16] in that direction is continuous at the FBZ boundary (e.g., TA→TO′ and LA→LO′ in Fig. 2 of Ref. 16), whereas along the ab plane the real dispersion relation shows some gaps at the FBZ boundary and has optical modes that are relatively slower compared to their acoustic counterparts.

The modeled specific heat of graphite is shown by the solid red line in Fig. 8(a), showing a transition from T^2 to T^0 behavior with increasing T, as expected from Table I as well as from standard models such as Lifshitz.[12] The model accounts for contributions from both optical and acoustic phonons, and we confirmed that the contribution from electrons is negligible at the temperatures considered here. The optical contributions are shown by the dashed red line and use $f_{E,\mathrm{LO/TO}} = 42$ THz and $f_{E,\mathrm{ZO}} = 23$ THz. The acoustic contribution was calculated using both approaches described above: summing over all three polarizations and using the two effective velocities calculated from Eqs. (21) and (22a). The two calculations are nearly indistinguishable, so only the former is shown in Fig. 8(a).

The experimental specific heat of graphite[3,4,31] is shown by the points in Fig. 8(a). With no free parameters the model agrees with the experimental data to within ±10% throughout the temperature range 50–2000 K. However, below 20 K the model transitions to a T^3 power law, which is too steep as compared to the experimental data. This discrepancy is due to the oversimplification of linearizing the phonon dispersion of the ZA branch. The literature dispersion[13,16] shows a monotonic decrease of the group velocity from 8500 m/s at the edge of the FBZ to approximately 1000 m/s at the Γ point. Therefore the secant method used here (6400 m/s) overestimates the velocity of small-wave-vector ZA phonons, which are the major contribution to the DOS at low temperatures, thereby underestimating their specific heat. A more detailed model dispersion such as Eq. (5) for the ZA branch[7,12,13,15,16] would help resolve this discrepancy, and also suggests an ideal T^1
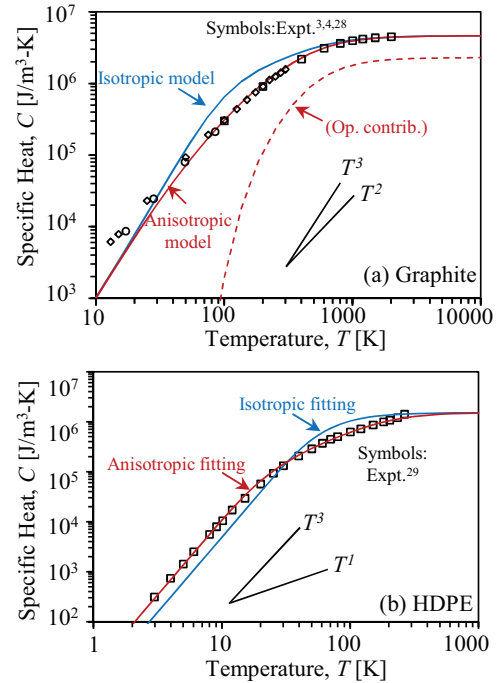

FIG. 8. (Color online) Comparison with experimental data for specific heat of (a) graphite and (b) HDPE, showing that the anisotropic Debye model successfully reproduces the specific heat of these strongly anisotropic materials. The model parameters for graphite are fully determined from the published dispersion relation without any fitting, while the HDPE model has two adjustable parameters because no published dispersion information was available.

regime between T^2 and T^0 for the ZA contribution to the specific heat.[12] However, such an approach is not pursued further here because it requires another material-dependent parameter which is less widely available, loses some of the simplicity and physical insight of the present model, and is not necessary for good accuracy at typical temperatures (∼50 K and above).

For comparison Fig. 8(a) also includes a traditional 3D isotropic Debye model (blue line). The isotropic sound velocity for each polarization is obtained using $v_{\mathrm{iso}} = (v_{ab}^2 v_c)^{\frac{1}{3}}$, as required by the low-temperature limit in Table I. Similarly, the isotropic cutoff wave vector k_D is calculated by conserving the number of acoustic modes, $k_D = (k_{ab,m}^2 k_{c,m})^{\frac{1}{3}}$. Thus, as shown in Fig. 8(a), this isotropic model exactly captures the same high-temperature Dulong and Petit limit and the low-temperature Debye T^3 law as the anisotropic model, but at intermediate temperatures the isotropic model misses the T^2 regime and overpredicts the heat capacity by more than a factor of 2.

C. Specific heat of high-density polyethylene

High-density polyethylene (HDPE) is chosen as a representative chainlike material because of its high anisotropy ($r \approx 0.09$) and the interest in its strongly direction-dependent and drawing-dependent thermal conductivity.[32,33]

The number density of HDPE primitive unit cells ($\eta_{\mathrm{puc}} = 3.64 \times 10^{28}$ m^{-3}) is estimated from the reported mass density[32] by approximating the primitive unit cell as containing

a single [CH$_2$] basis. However, the acoustic parameters needed to calculate the specific heat of HDPE are not well documented in the literature. Therefore the strategy here is to fit our model to the experimental data. We treat the two Debye temperatures $\theta_{D,ab}$ and $\theta_{D,c}$ as adjustable parameters and use a nonlinear least-squares algorithm[34] to minimize the rms error of [$(C_{\text{expt}} - C_{\text{model}})/C_{\text{expt}}$].

Figure 8(b) shows the experimental data and best-fit model for the specific heat of HDPE of crystallinity 0.77.[32] The experiment and model both show the expected transition from T^3 to T^1 behavior with increasing T, as expected from Table I. We note that a more detailed dispersion relation accounting for subcontinuum chain bending modes[12] suggests the T^1 regime of those modes may ideally be separated into $T^{5/2}$ and $T^{1/2}$ regimes, although those do not appear separately evident in the experimental data of Fig. 8(b). Returning to the present model, the T^0 Dulong and Petit regime is not expected until above 1000 K, which exceeds the melting temperature of HDPE ($\sim$400 K) and thus is not accessible in the experiments. Also, because the vibrational temperature of the C-H bond can be estimated as above 1800 K,[35] the heat capacity of the optical phonons is negligible over the entire experimental temperature range, and thus the calculation in Fig. 8(b) only accounts for the acoustic phonons. The fitting results show that the characteristic temperatures are $\theta_{D,ab} = 100$ K for the interchain modes and $\theta_{D,c} = 1099$ K for the intrachain modes, corresponding to a high anisotropy $r = 0.09$. For comparison, Fig. 8(b) also shows the best fit using a traditional 3D isotropic Debye model with one adjustable Debye temperature θ_D (289 K). The rms residual of the anisotropic model (7%) is much better than that of the isotropic model (48%).

D. Models for TBC and transmission coefficient

To calculate the TBC using Eq. (19), we need the irradiation and the transmission coefficients. The former has been discussed in detail in Sec. II D, and for the latter we now consider two common models: a maximum transmission model (MTM)[18] and a diffuse mismatch model (DMM).[2]

The MTM (or radiation limit) supplies for the TBC an extreme upper bound compatible with the second law of thermodynamics.[18] It assumes a 100% phonon transmission, leaving the material with the lesser H_c, and the opposite transmission coefficient can be obtained directly from Eq. (18), leading to a TBC,

$$G_{\text{MTM}} = \frac{2H_j}{H_j - H_i}\frac{\partial H_i}{\partial T}, \quad if\ H_i < H_j, \qquad (26)$$

where $i, j = A, B$ or equivalently B, A.

The DMM is often used as an estimate for atomically disordered interfaces. The key assumption is that phonons lose their memory after bombarding the interface, leading to a transmission coefficient of the form[2]

$$t_{ij,\text{DMM}}(T) = \frac{H_j(T)}{H_i(T) + H_j(T)}, \qquad (27)$$

where $i, j = A, B$ or equivalently B, A. Substituting Eq. (27) into Eq. (19), we obtain

$$G_{\text{DMM}} = 2\frac{\frac{\partial H_A}{\partial T}H_B^2 + \frac{\partial H_B}{\partial T}H_A^2}{(H_A + H_B)^2}. \qquad (28)$$

TABLE IV. Input parameters for metals. The number density of primitive unit cells n_{puc} is obtained from Ref. 17 and the velocities from Ref. 2, with the exception of the slightly anisotropic titanium for which the effective isotropic velocities are obtained from $v_{iso} = (v_{ab}^2 v_c)^{\frac{1}{3}}$, where v_{ab} and v_c are calculated from the stiffness constants.[11]

Material	n_{puc} $(10^{28}\ \text{m}^{-3})$	v_{LA} (m/s)	v_{TA} (m/s)
Al	6.02	6240	3040
Au	5.90	3390	1290
Cr	8.33	6980	4100
Ti	2.83	6105	2923

As noted previously, Eqs. (26) and (28) underline the symmetry of the heat transfer across the interface, i.e., there cannot be any thermal rectification upon exchanging the labels A and B.

We can now evaluate the suggestion from Sec. II that there may be a monotonic relationship between the irradiation and TBC. Without loss of generality, we fix H_A and increase H_B. For the DMM this does indeed always act to increase the TBC [Eqs. (19) and (27)]. However, for the MTM increasing H_B increases the TBC only while H_B is smaller than H_A, but for $H_B > H_A$ we see that increasing H_B reduces the TBC [Eq. (26)]. Thus the anticipated monotonic relationship between irradiation and TBC is always true for the DMM, although it is only sometimes true for the MTM.

E. TBC between graphite and metals

We now compare the TBC model to recent measurements by Schmidt *et al.*[5] for boundaries between highly ordered pyrolytic graphite (HOPG) and various metals. In all experiments the interfaces are aligned normal to the graphite's c axis, consistent with the model assumption. Using the input parameters for metals (Table IV) and those for graphite (Table III), the flux bombarding on the interfaces (H_c) from the graphite side is at most 16% of the flux from the metal sides throughout the experimental temperature range. This makes the overall TBC calculation dominated by graphite (particularly by the TL2 branch), as both Eqs. (26) and (28) simplify to $G \approx 2(\partial H_{c,gr}/\partial T)$ for $H_{c,gr} \ll H_{c,\text{metal}}$.

Figure 9 compares the experimental results[5] to four different models, including the traditional isotropic DMM,[2] the 2D-DOS DMM,[8] and the anisotropic DMM and MTM from this work. To facilitate meaningful comparisons, we underline two details held constant for all models. First, we include the prefactor τ [Eq. (17)], which we believe represents the real physics for the equilibrium temperature drop,[5,18,27] although it was not incorporated in the original 2D-DOS DMM.[8] This prefactor increases the modeled TBC by a factor of 2–3 [Eq. (19)]. Second, we assume inelastic transmission[27] across the interfaces. Although restricting the transmission to be purely elastic would reduce the modeled TBCs closer to the experimental results, it also introduces an ambiguity in matching the phonon branches of the metals to the hybrid branches of graphite (Sec. III A3).
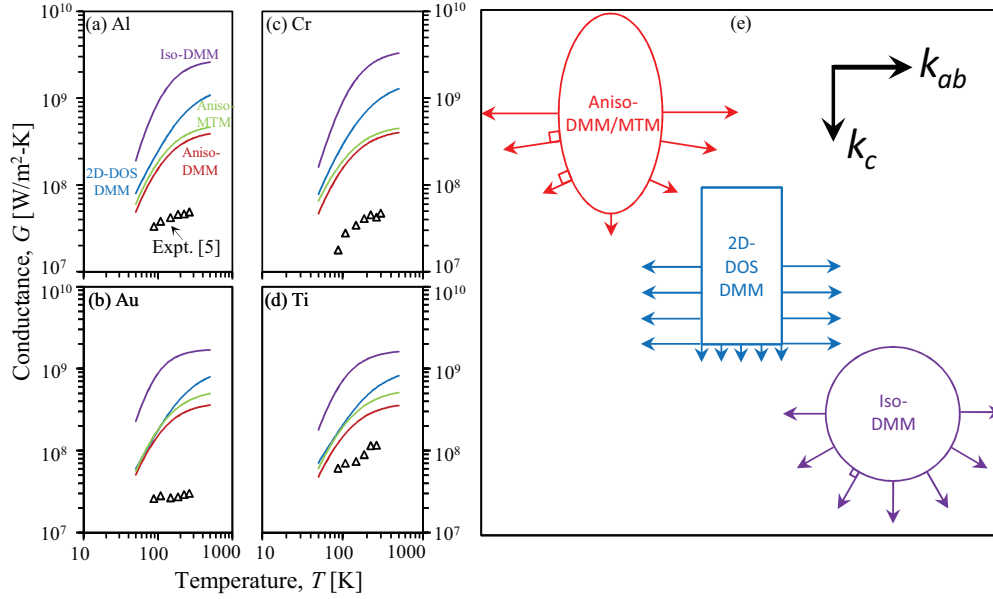
FIG. 9. (Color online) Comparison with experimental data[5] for TBC between graphite and (a) Al, (b) Au, (c) Cr, and (d) Ti. In each case, four different models are considered: the traditional isotropic DMM (Ref. [2]), the 2D-DOS DMM (Ref. [8]), and the anisotropic DMM and MTM from the present work. All models include the same prefactor [Eq. (17)] and assume inelastic transmission across interfaces. The corresponding rms errors are summarized in Table V. Key qualitative differences among the models are indicated by the isoenergy surfaces and group velocity vectors sketched in (e): as compared to the aniso-DMM, the 2D-DOS-DMM neglects the continuous transition from v_{ab} to v_c, while the iso-DMM is equivalent to decreasing v_{ab} and increasing v_c. In both cases, the additional approximations to v_{ab} and v_c tend to overestimate the c-axis heat transfer (Table II).

The rms errors of the four models as compared to the experimental data are summarized in Table V. None of the models had any parameters adjusted to improve their fits. The comparison shows that the experiments (points in Fig. 9) are best explained by the anisotropic DMM of the present work (red line), with an average error of 491%. The 2D-DOS DMM[8] (blue line) is the next-best model, with an average error of 1010%, while the traditional isotropic DMM (purple line)[2] is the worst, with an average error of 3464%. Although the average error of 491% for the anisotropic DMM certainly leaves something to be desired, disagreements of this magnitude and larger are common in TBC modeling, even of isotropic materials, and are most likely due to the failure of the DMM's fundamental assumptions about the interface transmissivity.[1]

Comparing the models in more detail, we note that the isotropic DMM predictions greatly exceed those of the anisotropic DMM, and the experimental data. This is because the averaging rule used to obtain an effective isotropic velocity, $v_{iso} = (v_{ab}^2 v_c)^{\frac{1}{3}}$, is equivalent to increasing the incident velocity v_c and decreasing the in-plane velocity v_{ab}. As shown in Table II, both of these changes tend to increase the irradiation in the c-axis direction, and as noted in Sec. III D, this will always correspond to an increase in the DMM TBC. The 2D-DOS DMM predictions exceed those of the anisotropic DMM for a similar reason, because the 2D-DOS DMM neglects the curvature of the isoenergy surface at the edge of the FBZ, which also has the effect of overestimating the group velocity component along the c-axis direction and thus increasing the TBC.

TABLE V. Comparison of rms errors ($\sqrt{\frac{1}{N} \sum [(G_{\text{expt}} - G_{\text{model}})/G_{\text{expt}}]^2}$) for the different TBC models shown in Fig. 8, indicating the improvement of the anisotropic models. For example, on average the anisotropic DMM is 7 times better than the standard isotropic DMM as compared to the experimental data.

Model	rms Al	rms Au	rms Cr	rms Ti	Avg
Aniso-DMM	462%	745%	599%	156%	491%
Aniso-MTM	569%	973%	715%	245%	626%
2D-DMM	1023%	1021%	1493%	324%	1010%
Iso-DMM	3512%	4408%	4807%	1129%	3464%
ratio: 2D-DMM/Aniso-DMM	2.2	1.6	2.5	2.1	2.1
ratio: Iso-DMM/Aniso-DMM	7.6	5.9	8.0	7.2	7.2

The other major feature of Fig. 9 is the implications of the anisotropic MTM (green line), which based on the second law of thermodynamics is expected to serve as an extreme upper bound for the TBC. The comparison with experiments shows that this anisotropic MTM indeed acts as an upper bound for these materials. However, Fig. 9 also shows that the isotropic DMM greatly exceeds the anisotropic MTM limit, indicating that approximating a strongly anisotropic material as isotropic can lead to TBC predictions that violate the second law of thermodynamics.

IV. SUMMARY AND CONCLUSIONS

We have developed a general framework to calculate the TBC for anisotropic materials based on an anisotropic Debye dispersion relation and ellipsoidal first Brillouin zone, which also yields compact analytical expressions in various limiting cases. When compared to the experimental TBC between graphite and various metals from the literature,[5] the new anisotropic DMM has errors at least a factor of 6 smaller than those of the traditional isotropic DMM and errors typically 2 times smaller than those of a recent 2D-DOS DMM.[8] The anisotropic model also predicts an interesting and unexpected guideline for materials engineering to increase the TBC: due to phonon focusing the TBC actually can be increased by reducing a phonon velocity, as long as it is a velocity component parallel to the plane of the interface. Recently an analogous effect on the thermal conductivity has also been reported.[22–25]

APPENDIX A: EVALUATING THE DOS AND vDOS INTEGRALS

The general form of the DOS [Eq. (10)] is a surface integral[36] which can be evaluated by projecting the 3D isoenergy surface to a 2D plane. Here we project it to the k_a-k_b plane:

$$\iint \frac{dS_\omega}{\|\mathbf{v}_g\|} = \iint \sqrt{1 + \left(\frac{\partial k_c}{\partial k_a}\right)^2 + \left(\frac{\partial k_c}{\partial k_b}\right)^2} \frac{dk_a dk_b}{\|\mathbf{v}_g\|}, \quad (A1)$$

where k_c can be expressed in terms of k_a and k_b:

$$k_c = \sqrt{\omega^2 - v_{ab}^2\left(k_a^2 + k_b^2\right)}/v_c. \quad (A2)$$

Equation (A1) can be evaluated by implementing the polar-coordinate substitution:

$$k_a = \rho \cos\varphi, \quad k_b = \rho \sin\varphi, \quad (A3)$$

where the domain of the polar angle is $0 \leqslant \varphi \leqslant 2\pi$. The main complication is in determining the domain of the polar radius ρ.
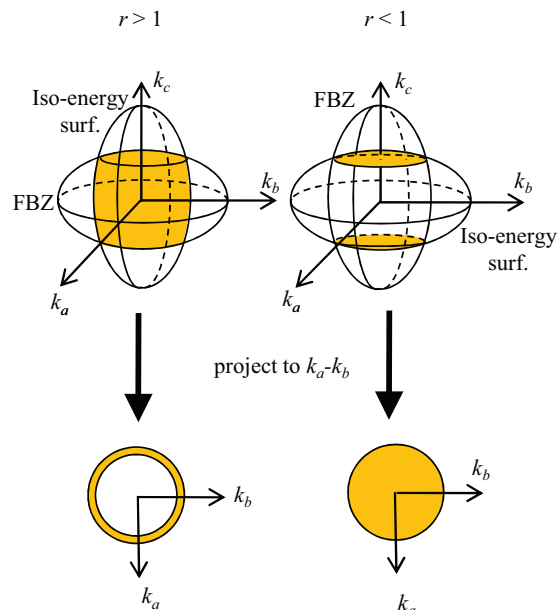

FIG. 10. (Color online) Mathematical framework to evaluate Eq. (10) for $\min(\omega_{D,c},\omega_{D,ab}) < \omega < \max(\omega_{D,c},\omega_{D,ab})$. For materials with anisotropy ratio $r > 1$, the k_a-k_b projection of the isoenergy surface within the FBZ is an annulus. For materials with $r < 1$, the projection of the isoenergy surface becomes instead a disk.

When $\omega < \min(\omega_{D,c},\omega_{D,ab})$, no part of the isoenergy surface has reached the boundary of the FBZ, so $0 \leqslant \rho \leqslant \omega/v_{ab}$. However, when $\min(\omega_{D,c},\omega_{D,ab}) < \omega < \max(\omega_{D,c},\omega_{D,ab})$, part of the isoenergy surface lies outside of the FBZ, and it is helpful to consider the domain of ρ in two categories. First, for materials with anisotropy ratio $r > 1$, the k_a-k_b projection of the isoenergy surface within the FBZ is an annulus (Fig. 10), with an outer radius $\rho_{\max} = \omega/v_{ab}$ and an inner radius $\rho_{\min} = k_{ab,m}\sqrt{(\omega_{D,ab}^2 - \omega^2)/(\omega_{D,ab}^2 - \omega_{D,c}^2)}$, which can be obtained by solving the intersection of the two ellipsoids in Fig. 10. Second, for materials with $r < 1$, the projection of the isoenergy surface becomes instead a disk (Fig. 10), with $\rho_{\max} = k_{ab,m}\sqrt{(\omega_{D,c}^2 - \omega^2)/(\omega_{D,c}^2 - \omega_{D,ab}^2)}$, again obtained from the intersection of the two ellipsoids in Fig. 10.

Having identified the appropriate domain of ρ, it is straightforward to evaluate the polar-coordinate version of Eq. (A1), and thus the DOS. For layered materials ($r > 1$) we find

$$D(\omega) = \begin{cases} \frac{\omega^2}{2\pi^2 v_{ab}^2 v_c}, & 0 \leqslant \omega \leqslant \omega_{D,c} \\ \frac{\omega}{2\pi^2 v_{ab}^2 v_c}\sqrt{\frac{\omega_{D,c}^2(\omega_{D,ab}^2 - \omega^2)}{\omega_{D,ab}^2 - \omega_{D,c}^2}}, & \omega_{D,c} \leqslant \omega \leqslant \omega_{D,ab} \end{cases}. \quad (A4)$$

For chainlike materials ($r < 1$),

$$D(\omega)$$
$$= \begin{cases} \frac{\omega^2}{2\pi^2 v_{ab}^2 v_c}, & 0 \leqslant \omega \leqslant \omega_{D,ab} \\ \frac{\omega^2}{2\pi^2 v_{ab}^2 v_c} - \frac{\omega}{2\pi^2 v_{ab}^2 v_c}\sqrt{\frac{\omega_{D,c}^2(\omega^2 - \omega_{D,ab}^2)}{\omega_{D,c}^2 - \omega_{D,ab}^2}}, & \omega_{D,ab} \leqslant \omega \leqslant \omega_{D,c} \end{cases}. \quad (A5)$$

(a) 2D phonon gas
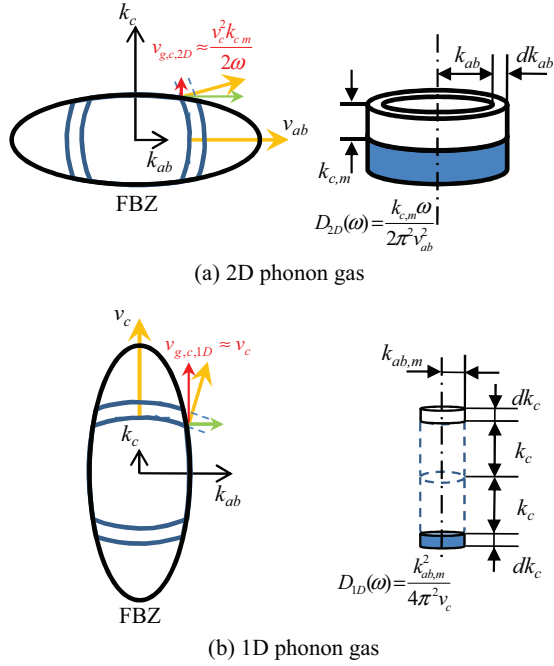

(b) 1D phonon gas

FIG. 11. (Color online) 2D and 1D phonon gas models to verify the specific heat and c-axis irradiation of strongly anisotropic materials at intermediate temperatures $[\min(\theta_{D,c}, \theta_{D,ab}) \ll T \ll \max(\theta_{D,c}, \theta_{D,ab})]$. The two key features are the DOS and the c-axis component of the group velocity.

Following a similar procedure, we evaluate the vDOS also in two categories. For $r > 1$,

$$h_c(\omega) = \begin{cases} \dfrac{\omega^2}{8\pi^2 v_{ab}^2}, & 0 \leqslant \omega \leqslant \omega_{D,c} \\ \dfrac{\omega_{D,c}^2}{8\pi^2 v_{ab}^2} \dfrac{\omega_{D,ab}^2 - \omega^2}{\omega_{D,ab}^2 - \omega_{D,c}^2}, & \omega_{D,c} \leqslant \omega \leqslant \omega_{D,ab} \end{cases}, \quad \text{(A6)}$$

and for $r < 1$,

$$h_c(\omega) = \begin{cases} \dfrac{\omega^2}{8\pi^2 v_{ab}^2}, & 0 \leqslant \omega \leqslant \omega_{D,ab} \\ \dfrac{\omega_{D,ab}^2}{8\pi^2 v_{ab}^2} \dfrac{\omega_{D,c}^2 - \omega^2}{\omega_{D,c}^2 - \omega_{D,ab}^2}, & \omega_{D,ab} \leqslant \omega \leqslant \omega_{D,c} \end{cases}. \quad \text{(A7)}$$

APPENDIX B: 2D AND 1D PHONON GAS MODELS

Here we develop simplified 2D and 1D phonon gas models to verify the various intermediate-T limiting behaviors presented above for the specific heat (Table I) and c-axis irradiation (Table II). The 2D and 1D DOS (Fig. 11) for a single polarization are easily shown to be

$$D(k_{ab}) = \frac{1}{2\pi^2} k_{ab} k_{c,m} \text{ (2D)}, \quad D(k_c) = \frac{1}{4\pi^2} k_{ab,m}^2 \text{ (1D)}. \quad \text{(B1)}$$

Conservation of the number of modes requires

$$D(k_{ab})dk_{ab} = D(\omega)d\omega \text{ (2D)}, \quad D(k_c)dk_c = D(\omega)d\omega \text{ (1D)}, \quad \text{(B2)}$$

and the group velocity components along the ab plane and c axis are

$$v_{g,ab} = v_{ab}^2 k_{ab}/\omega \text{ (2D)}, \quad v_{g,c} = v_c^2 k_c/\omega \text{ (1D)}. \quad \text{(B3)}$$

Combining these we obtain the frequency-dependent DOS,

$$D_{2D}(\omega) = \frac{k_{c,m}\omega}{2\pi^2 v_{ab}^2}, \quad D_{1D}(\omega) = \frac{k_{ab,m}^2}{4\pi^2 v_c}. \quad \text{(B4)}$$

Substituting Eq. (B4) into Eq. (11), we obtain the 2D and 1D specific heat:

$$C_{2D} = \frac{3\zeta_3 k_B^3 k_{c,m}}{\pi^2 \hbar^2} \sum_{\text{pol}} \frac{T^2}{v_{ab}^2}, \quad C_{1D} = \frac{k_{ab,m}^2 k_B^2}{12 v_c \hbar} \sum_{\text{pol}} \frac{T}{v_c}, \quad \text{(B5)}$$

which agrees with the limiting behaviors in Table I. The 2D and 1D irradiation along the c axis can be calculated from

$$H_c = \sum_{\text{pol}} \int_\omega \hbar\omega f_{BE} \frac{1}{2} D v_{g,c} d\omega. \quad \text{(B6)}$$

The prefactor $\frac{1}{2}$ arises because only the states with a wave-vector component $k_c < 0$ are involved in this transport process. In the following discussion, we focus on the simplification of $v_{g,c}$.

For the 2D phonon gas [Fig. 11(a)], we have

$$\omega \simeq v_{ab} k_{ab}. \quad \text{(B7)}$$

Combining Eqs. (B3) and (B7) and averaging $v_{g,c}$ over the range $[-k_{c,m}, 0]$, we find

$$v_{g,c,2D} \approx \frac{v_c^2 k_{c,m}}{2\omega}. \quad \text{(B8)}$$

Substituting Eq. (B8) into Eq. (B6), we obtain the 2D irradiation along the c axis,

$$H_{c,2D} = \frac{k_{c,m}^2 k_B^2 T^2}{48\hbar} \sum_{\text{pol}} \frac{v_c^2}{v_{ab}^2}, \quad \text{(B9)}$$

which agrees with the limiting behavior in Table II.

Likewise, for a 1D phonon gas [Fig. 11(b)], we have

$$\omega \approx v_c k_c. \quad \text{(B10)}$$

Combining Eqs. (B3) and (B10), we find

$$v_{g,c,1D} \approx v_c. \quad \text{(B11)}$$

Substituting Eq. (B11) into Eq. (B6), we obtain the 1D irradiation along the c axis,

$$H_{c,1D} = \frac{k_{ab,m}^2 k_B^2 T^2}{16\hbar}, \quad \text{(B12)}$$

which again agrees with the limiting behavior in Table II.

APPENDIX C: DEFINING AN EQUILIBRIUM TEMPERATURE

As mentioned in Ref. 18, there are several ways to define an equilibrium temperature T_{eq} in terms of the opposing emitted temperatures T_+ and T_- used in a two-flux model. The typical strategy is to require conservation of some related quantity such as phonon number density, energy density, or irradiation along the c axis. Here we show that the difference between any of these definitions and a naive definition

$$T_{\text{eq,naive}} = \frac{1}{2}(T_+ + T_-) \quad \text{(C1)}$$

is of the order of Δ^2/T_-, where $\Delta = T_+ - T_-$, and thus for low-to-moderate thermal bias all definitions are practically equivalent.

Here we take the conservation of irradiation along the c axis as an example:

$$H_c(T_{eq}) = \tfrac{1}{2} H_c(T_+) + \tfrac{1}{2} H_c(T_-). \tag{C2}$$

In the analytical limiting cases in Table II, we have

$$H_c(T) = A T^n, \tag{C3}$$

where A is a function of the velocities and wave-vector cutoffs, but not temperature. For intermediate cases not covered by Table II, the numerical results of Fig. 6 confirm that H_c is a smoothly varying function of T, which for small Δ around any T is still well approximated by the power-law form of Eq. (C3). Therefore n is in the range [1, 4], though not necessarily an integer.

Substituting Eq. (C3) into Eq. (C2), the equilibrium temperature can be generalized as

$$T_{eq}^n = \tfrac{1}{2} T_+^n + \tfrac{1}{2} T_-^n. \tag{C4}$$

Using a Taylor series Eq. (C4) can be expanded as

$$T_{eq} = T_- \left[1 + \frac{\Delta}{2T_-} + \frac{n-1}{8}\left(\frac{\Delta}{T_-}\right)^2 + O\left(\frac{\Delta}{T_-}\right)^3 \right], \tag{C5}$$

where O represents higher-order terms. The naive arithmetic average equilibrium temperature can be expressed as

$$T_{eq,naive} = T_- \left(1 + \frac{\Delta}{2T_-} \right). \tag{C6}$$

Subtracting Eq. (C6) from Eq. (C5) and neglecting higher-order terms, we obtain

$$\frac{T_{eq} - T_{eq,naive}}{T_{eq}} \approx \frac{\frac{n-1}{8}\left(\frac{\Delta}{T_-}\right)^2}{1 + \frac{\Delta}{2T_-} + \frac{n-1}{8}\left(\frac{\Delta}{T_-}\right)^2}. \tag{C7}$$

Considering that $\Delta/T_- \ll 1$, Eqs. (C5) and (C7) indicate that $(T_{eq} - T_{eq,naive})/T_{eq} \ll \Delta/T_{eq}$, and thus the naive definition is adequate to represent the real equilibrium temperature.

Following a similar procedure, we have confirmed that the conclusion above also applies to approaches using conservation of phonon number density and energy density.

APPENDIX D: COMPARISON TO THE PHONON IRRADIATION CALCULATED USING FULL DIRECTION DISPERSION

As discussed in Sec. III E, we believe the discrepancies between the anisotropic DMM model and the experimental TBC seen in Fig. 9 are largely due to the crude approximations for the transmission coefficients, not the anisotropic Debye
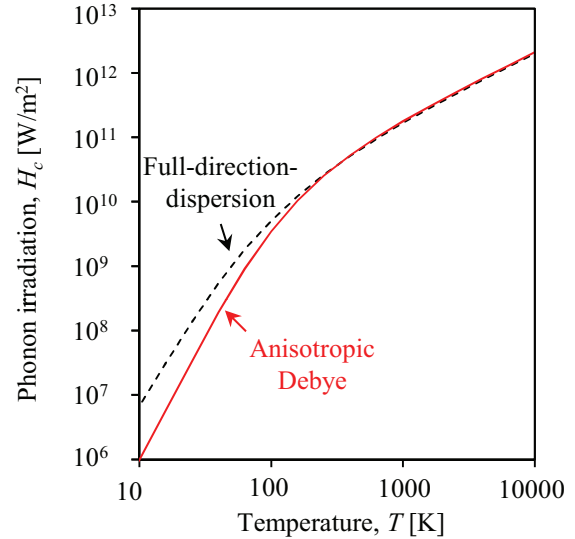

FIG. 12. (Color online) Comparison with lattice dynamics calculation (all-direction-dispersion) for phonon irradiation of a graphite-like material, showing errors less than 10% from 200 K to 10 000 K. The disagreement at lower temperature is due to the failure to capture the reduced group velocity of ZA phonons at long wavelengths.[12] The Debye model parameters for this graphitelike material are fully determined from the dispersion calculated from the lattice dynamics method[22] without any fitting.

approximation used for the phonon irradiation. To independently check the H_c calculation, here we validate the anisotropic Debye model by comparison with the phonon irradiation of a graphitelike material calculated using the lattice dynamics method.[22,37] We followed Ref. 22 in detail, including using the optimized Tersoff potential[38] for intraplane interactions and the Lennard-Jones (LJ) potential[39] for interplane interactions. With the resulting all-direction dispersion relation, we calculated the phonon irradiation by modifying Eq. (2) in Ref. 22 from classical to Bose-Einstein statistics.

Figure 12 shows the comparison between the phonon irradiation calculated using the lattice dynamics dispersion and that calculated using our model with velocities ($v_{ab,TA} = 10\,100$, $v_{ab,TL1} = 25\,000$, $v_{ab,TL2} = 5700$; $v_{c,TA} = 300$, $v_{c,TL1} = 300$, $v_{c,TL2} = 2500$ [m/s]) extracted from the lattice dynamics dispersion along [100] and [001]. The simple Debye ellipsoid results agree with the full lattice dynamics calculation to within $\pm 10\%$ over a wide temperature range from 200 to 10 000 K. Below 100 K, the Debye ellipsoid approximation deviates from the lattice dynamics results due to the shortcoming described in Sec. II A: for the ZA branch, the Debye model cannot capture the dependence of phase velocity on the magnitude of the wave vector.

*To whom correspondence should be addressed: cdames@berkeley.edu

[1] D. G. Cahill, W. K. Ford, K. E. Goodson, G. D. Mahan, A. Majumdar, H. J. Maris, R. Merlin, and S. R. Phillpot, J. Appl. Phys. **93**, 793 (2003).

[2] E. T. Swartz and R. O. Pohl, Rev. Mod. Phys. **61**, 605 (1989).

[3] W. DeSorbo and W. W. Tyler, J. Chem. Phys. **21**, 1660 (1953).

[4] U. Bergenlid, R. W. Hill, F. J. Webb, and J. Wilks, Philos. Mag. **45**, 851 (1954).

[5] A. J. Schmidt, K. C. Collins, A. J. Minnich, and G. Chen, J. Appl. Phys. **107**, 104907 (2010).

[6] R. Prasher, Phys. Rev. B **77**, 075424 (2008).

[7] K. Komatsu, J. Phys. Soc. Jpn. **10**, 346 (1955).

[8] J. C. Duda, J. L. Smoyer, P. M. Norris, and P. E. Hopkins, Appl. Phys. Lett. **95**, 031912 (2009).

[9] J. C. Bowman and J. A. Krumhansl, J. Phys. Chem. Solids **6**, 367 (1958).

[10] K. Kopinga, P. van der Leeden, and W. J. M. de Jonge, Phys. Rev. B **14**, 1519 (1976).

[11] B. A. Auld, *Acoustic Fields and Waves in Solids* (Wiley, New York, 1973).

[12] L. D. Landau and E. M. Lifshitz, *Statistical Physics* (Pergamon, New York, 1980).

[13] R. Nicklow, N. Wakabayashi, and H. G. Smith, Phys. Rev. B **5**, 4951 (1972).

[14] R. Saito, A. Jorio, A. G. Souza Filho, G. Dresselhaus, M. S. Dresselhaus, and M. A. Pimenta, Phys. Rev. Lett. **88**, 027401 (2001).

[15] G. Savini, Y. J. Dappe, S. Öberg, J. C. Charlier, M. I. Katsnelson, and A. Fasolino, Carbon **49**, 62 (2011).

[16] L. Wirtz and A. Rubio, Solid State Commun. **131**, 141 (2004).

[17] C. Kittel, *Introduction to Solid State Physics* (John Wiley & Sons, New York, 1996).

[18] C. Dames and G. Chen, J. Appl. Phys. **95**, 682 (2004).

[19] T. Klitsner, J. E. VanCleve, H. E. Fischer, and R. O. Pohl, Phys. Rev. B **38**, 7576 (1988).

[20] J. P. Wolfe, *Imaging Phonons: Acoustic Wave Propagation in Solids* (Cambridge University Press, New York, 1998).

[21] N. Zuckerman and J. R. Lukes, J. Heat Transfer **130**, 082402 (2008).

[22] Z. Wei, Y. Chen, and C. Dames, Appl. Phys. Lett. **102**, 011901 (2013).

[23] P. K. L. Hu, S. Shenogin, and D. Cahill (unpublished); cited in Refs. 24 and 25.

[24] C. Chiritescu, D. G. Cahill, C. Heideman, Q. Lin, C. Mortensen, N. T. Nguyen, D. Johnson, R. Rostek, and H. Bottner, J. Appl. Phys. **104**, 033533 (2008).

[25] W.-P. Hsieh, B. Chen, J. Li, P. Keblinski, and D. G. Cahill, Phys. Rev. B **80**, 180302 (2009).

[26] M. F. Modest, *Radiative Heat Transfer* (McGraw-Hill, New York, 1993).

[27] G. Chen, Phys. Rev. B **57**, 14958 (1998).

[28] G. Chen, *Nanoscale Energy Transport and Conversion* (Oxford University Press, New York, 2005).

[29] T. Beechem and P. E. Hopkins, J. Appl. Phys. **106**, 124301 (2009).

[30] J. Krumhansl and H. Brooks, J. Chem. Phys. **21**, 1663 (1953).

[31] F. P. Incropera, D. P. DeWitt, T. L. Bergman, and A. S. Lavine, *Introduction to Heat Transfer* (John Wiley & Sons, New York, 2007).

[32] D. B. Mergenthaler and M. Pietralla, Z. Phys. B **94**, 461 (1994).

[33] S. Shen, A. Henry, J. Tong, R. Zheng, and G. Chen, Nat. Nanotechnol. **5**, 251 (2010).

[34] S. C. Chapra, *Applied Numerical Methods with Matlab* (McGraw-Hill, New York, 2008).

[35] V. P. Carey, *Statistical Thermodynamics and Microscale Thermophysics* (Cambridge University Press, New York, 1999).

[36] M. D. Greenberg, *Advanced Engineering Mathematics* (Prentice Hall, New Jersey, 1998).

[37] M. T. Dove, *Introduction to Lattice Dynamics* (Cambridge University Press, Cambridge, 1993).

[38] L. Lindsay and D. A. Broido, Phys. Rev. B **81**, 205441 (2010).

[39] L. A. Girifalco, M. Hodak, and R. S. Lee, Phys. Rev. B **62**, 13104 (2000).